

## Ion two-stream instabilities in the auroral acceleration zone

L. Muschietti<sup>1</sup> and I. Roth<sup>1</sup>

Received 20 December 2007; revised 6 March 2008; accepted 16 April 2008; published 1 August 2008.

[1] Ion beams streaming upward out of the ionosphere are frequently observed in the auroral acceleration cavity. They mainly consist of  $H^+$  and  $O^+$  ions drifting along the magnetic field lines and are believed to have been accelerated upward by the same parallel potential drop at the transition from the topside ionosphere. Due to the mass difference,  $H^+$  and  $O^+$  form two distinct beams drifting at different speeds, whereby two-stream instabilities may develop. Here we present 1D and 2D PIC simulations of the interaction between the  $H^+$  and  $O^+$  beams in the cavity. Our model describes an open system, where a population of hot plasma sheet protons and hot electrons is at rest while  $H^+$  and  $O^+$  are constantly injected at the boundary, emulating thus the ion influx from the bottom of the cavity. The study's results indicate two regimes according to the kinetic energy of the injected beams. For moderate energies the unstable waves are of the acoustic type and propagate parallel to the magnetic field. They can trap  $H^+$  and  $O^+$  ions, leading to phase-space vortices and the accompanying signatures of ion solitary waves in the electric field. For larger energies, the parallel acoustic waves are replaced by oblique cyclotron waves. The latter waves crisscross, forming a herringbone pattern that energizes the  $O^+$  ions perpendicularly and leads to drifting conics. By contrast, the protons are hardly energized perpendicularly. The transition between the two regimes depends upon the electron temperature and the ion composition. In either case energy is transferred from the protons to the oxygens.

**Citation:** Muschietti, L., and I. Roth (2008), Ion two-stream instabilities in the auroral acceleration zone, *J. Geophys. Res.*, 113, A08201, doi:10.1029/2007JA013005.

### 1. Introduction

[2] The coupling of the dense and cold ionospheric plasma to the tenuous and warm magnetospheric plasma constitutes a major research theme of auroral physics. In upward-current regions of the auroral zone, it is believed that a strong double layer localized within ten Debye lengths [Ergun *et al.*, 2002] marks the transition from the topside ionosphere to a so-called auroral cavity where the plasma is an order of magnitude more tenuous (less than one particle per cc). The double layer includes a dc parallel electric field which accelerates cold ions from the ionosphere into the cavity. There, they are observed as beams made of  $H^+$  and  $O^+$  which drift upward along the magnetic field lines. Having been accelerated upward by the same potential,  $H^+$  and  $O^+$  form in fact two distinct beams that drift at different speeds due to the mass difference, whereby two-stream instabilities can develop. Other particle populations in the cavity include energetic plasma sheet protons and inverted V electrons of magnetospheric origin which, except for the loss cone, are isotropic in pitch angle.

[3] We present 1D and 2D PIC (particle-in-cell) simulations of the interaction between the  $H^+$  and  $O^+$  beams

relevant to the auroral cavity. Our simulation model has its main axis oriented parallel to the magnetic field lines and describes an open system where protons and oxygen ions of ionospheric origin are (1) constantly injected at the lower boundary, emulating thus the ion influx from the bottom of the cavity, and (2) mainly lost at the upper boundary. The other populations, such as plasma sheet protons and hot electrons, are injected/lost at both lower and upper boundaries. As for the “side boundaries” present in the 2D simulations, they are assumed periodic.

[4] Electric field instruments onboard satellites traversing the auroral cavity frequently measure ion cyclotron waves and nonlinear wave structures. The cyclotron waves were first identified in the broadband electric field data from the S3-3 satellite as electrostatic proton cyclotron waves [Kintner *et al.*, 1978]. At lower altitude, 4000 km, FAST recorded waves near the cyclotron frequencies of  $H^+$ ,  $O^+$ , and  $He^+$  [Cattell *et al.*, 1998]. Chaston *et al.* [2002] studied in detail proton cyclotron waves located in the auroral cavity. They showed that the waves include an electromagnetic component and concluded that they are destabilized by a field-aligned component in the electron distribution. The electric field amplitude is typically on the order of 100 mV/m, yet can reach several times more and exhibit nonsinusoidal waveforms.

[5] The nonlinear wave structures, dubbed ion solitary waves and weak double layers, are identified by a bipolar electric signal parallel to the magnetic field with a charac-

<sup>1</sup>Space Sciences Laboratory, University of California, Berkeley, California, USA.

**Table 1.** Species Parameters in Normalized Units

Name	Protons	Oxygens	PS-Protons	Electrons
Gyrofrequency	$\Omega_H = 1.$	$\Omega_O = 0.0625$	$\Omega_{ps} = 1.$	$\Omega_e = 100.$
Gyroradius	$\rho_H = 1.$	$\rho_O = 4.$	$\rho_{ps} = 15.$	$\rho_e = 0.5$
Thermal velocity	$v_H = 1.0$	$v_O = 0.25$	$v_{ps} = 15.$	$v_e = 50.$
Plasma frequency	$\omega_H = 0.43$	$\omega_O = 0.1075$	$\omega_{ps} = 0.43$	$\omega_e = 7.448$
Drift speed				
Case A	$V_H = 5.66$	$V_O = 1.415$	none	none
Case B	$V_H = 9.$	$V_O = 2.25$	none	none

teristic time of order 10 ms. They were first observed by the S3-3 satellite [Temerin *et al.*, 1982] and measured in more details later by Viking [Bostrom *et al.*, 1988]. The ion solitary wave is distinguished from the fast solitary wave which has a much shorter characteristic time of order 0.2 ms and is typically seen in the downward-current region [Ergun *et al.*, 1998]. Equally important from a theoretical viewpoint, the two types can be distinguished according to the polarity of the underlying potential whose passage by the satellite creates the bipolar electric signal. The potential hump is positive in the case of a fast solitary wave, whereas it is negative for an ion solitary wave. In the latter case the solitary wave is also observed as rarefactive, being associated with a localized density depletion in the plasma. Recent investigations of the high- and midaltitude auroral zone by satellites with more capable electric field instruments such as Polar and FAST [Bounds *et al.*, 1999; Dombeck *et al.*, 2001; McFadden *et al.*, 2003] have definitely associated the ion solitary waves (ISWs hereafter) with the upflowing ion beams present in the upward-current region. Not only are they observed simultaneously, yet also ISWs have propagation speeds on the order of the ion beams, typically hundreds of km/s.

[6] Previous studies of the interaction between  $H^+$  and  $O^+$  beams include linear analysis of the instability in 1D and 2D [Bergmann and Lotko, 1986; Bergmann *et al.*, 1988], and PIC simulations of the nonlinear development of oblique cyclotron waves [Roth *et al.*, 1989]. The latter were performed with a 1D setup oriented at an angle to the magnetic field and incorporated periodic boundary conditions. Subsequently, Crumley *et al.* [2001], using a 2D PIC code also with periodic boundary conditions, tried to simulate the formation of ISWs as a result of an  $H^+ - O^+$  instability. Most recently, Main *et al.* [2006] investigated the transition between the ionosphere and the auroral cavity by means of 1D and 2D Vlasov codes. Since they used nonperiodic boundaries, the authors were able to include a double layer in the simulation box. Their work demonstrates that a BGK double layer at the lower boundary is stable and leads to the continual acceleration of drifting ionospheric  $H^+$  and  $O^+$  ions into the cavity.

[7] In this article we investigate the interaction between the  $H^+$  and  $O^+$  beams using 1D and 2D PIC codes with open boundary conditions. The setup has its main axis oriented parallel to the magnetic field lines and, in the 2D case, is designed to describe parallel acoustic waves and oblique, short-wavelength cyclotron waves at once. We show that there are two regimes according to the kinetic energy of the injected beams: a low-drift regime and a high-drift regime, where the transition energy is roughly on the order of the electron temperature  $T_e$ . For moderate energies (less than  $T_e$ ), the relative drift between  $H^+$  and  $O^+$  ions is such that

the unstable waves are of the acoustic type and propagate parallel to the magnetic field. For larger energies, the relative drift between the two species is too fast for the acoustic waves to develop. Instead, oblique oxygen cyclotron waves grow unstable. Two cases exemplify the two regimes with specific parameter values: Case A for the low drift and Case B for the high drift. For beams with energies close to the transition energy the simulated wave field is more complex, exhibiting a mix of acoustic and cyclotron instabilities. Tables 1 and 2 present the various parameters that characterize the simulations in dimensionless units as well as in physical units. The choice of values is inspired by the measurements of FAST at altitudes near 4000 km [McFadden *et al.*, 1999]. Table 1 gives the parameters in our normalized units, which we base on the beam protons. Time is in units of the inverse proton cyclotron frequency  $\Omega_H^{-1}$ , velocity is in units of the thermal velocity of an injected proton  $v_H = (T_H/M_H)^{1/2}$ , and distance in units of its gyroradius  $\rho_H$ . Table 2 presents the parameters in physical units. Under these conditions, the electron Debye length is equal to  $\lambda_e = 490$  m, or  $6.71 \rho_H$  in our normalized unit. The unusual ordering between  $\lambda_e$  and  $\rho_H$  is due to the fact that the auroral cavity mixes hot magnetospheric electrons and cold ionospheric protons within a strongly magnetized environment.

## 2. Dispersion Relation

[8] The classic two-stream instability arises where two cold populations stream with respect to each other. If the two populations comprise electrons only or electrons and ions, there is no limit to how large the relative drift can be. Simply, as the drift increases, the unstable wavenumber decreases proportionally. The situation, on the other hand, is different for two ion beams streaming past each other. The reason for the difference is that this case in fact involves the dynamics of a third population of highly mobile particles, such as electrons, which provide the screening. For long wavelengths the screening is perfect, so that the two beams “ignore” each other. In the plasma environment of the auroral cavity, the screening is provided by the electrons and also by a population of plasma sheet protons. The latter are nearly isotropic and have thermal velocities on the order of 1000 km/s, hence larger than the speeds of the  $H^+$  or  $O^+$  beams (see Table 2).

### 2.1. Speed Limit

[9] Let us first consider the simplest form of the dielectric relevant to the problem of interest,

$$\epsilon = 1 + \frac{\omega_e^2}{k^2 v_e^2} + \frac{\omega_{ps}^2}{k^2 v_{ps}^2} - \frac{\omega_H^2}{(\omega - kV_H)^2} - \frac{\omega_O^2}{(\omega - kV_O)^2}. \quad (1)$$

**Table 2.** Species Parameters in Physical Units

Name	Protons	Oxygens	PS-Protons	Electrons
Gyrofrequency, rad/s	958	59.9	958	$1.76 \times 10^6$
Temperature, eV	52	52	11,720	1305
Density, $\text{cm}^{-3}$	0.1	0.1	0.1	0.3
Drift speed, km/s				
Case A	400	100	none	none
Case B	636	159	none	none

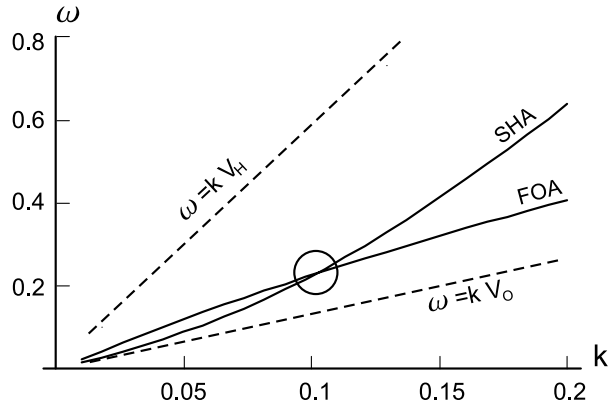


**Figure 1.** Schematic of the dispersion for acoustic-acoustic coupling. Doppler frequencies of the two beams,  $H^+$  and  $O^+$ , are indicated by dashed lines. The slow acoustic mode of the faster,  $H^+$  beam (marked SHA) crosses the fast acoustic mode of the  $O^+$  beam (marked FOA), leading to an instability. Units:  $H^+$  gyrofrequency and gyroradius. Parameters in Table 1, Case A.

Here  $v_e$ ,  $v_{ps}$  denote the thermal velocities of the electrons and plasma sheet protons, which are assumed at rest. Further,  $V_H$ ,  $V_O$  denote the drifts of the proton and oxygen beams, respectively. Some characteristic values are given in Table 2. Equation (1) is one-dimensional along the magnetic field and neglects the thermal spread of the ionospheric ions assuming that the acceleration in the dc electric field leads to drifts larger than the thermal speeds. One may lump together the two screening terms by defining a modified Debye length  $\lambda_d \equiv (v_e/\omega_e)\Psi$  where the correction factor

$$\Psi \equiv (1 + r_{ps}T_e/T_{ps})^{-1/2} \quad (2)$$

is contributed by the population of plasma sheet protons whose relative density is denoted by  $r_{ps} \equiv n_{ps}/n_e$ . The dielectric thus becomes

$$\epsilon = 1 + \frac{1}{k^2\lambda_d^2} - \frac{\omega_H^2}{(\omega - kV_H)^2} - \frac{\omega_O^2}{(\omega - kV_O)^2}. \quad (3)$$

Although the effect of  $\Psi$  is to decrease the screening length scale, we note that  $\Psi$  is close to unity,  $\Psi \lesssim 1$  in fact, after using values in Table 2 for the densities and temperatures. Setting  $\epsilon \equiv 0$  in (3) yields four simultaneous roots. To each beam,  $\alpha = H, O$ , are associated two acoustic beam modes:

$$\omega(k) = kV_\alpha \pm kC_{s\alpha} \left( \frac{1 - r_{ps}}{1 + k^2\lambda_d^2} \right)^{1/2}. \quad (4)$$

Here the acoustic speed is defined as  $C_{s\alpha} \equiv (T_e/M_\alpha)^{1/2}\Psi$ . Now if for some wavenumber the slow acoustic mode (− sign in (4)) of the faster, proton beam crosses the fast acoustic mode (+ sign in (4)) of the slower oxygen beam, the two modes can couple, resulting in an instability. The case is illustrated in Figure 1. The two dashed lines indicate the Doppler frequency of the beams. The slow acoustic mode carried by the hydrogen beam (solid line marked

SHA) intersects the fast acoustic mode carried by the oxygen beam (solid line marked FOA) at the point indicated by a circle.

[10] Two remarks are in order. First, to have a crossing, some curvature in the branch  $\omega(k)$  is needed. This demands  $k\lambda_d \sim 1$ , hence the interaction cannot happen for small wavenumbers. Thus we expect the instability to have a short wavelength that is not much smaller than the Debye length. Consider for example the situation in Figure 1 that has been drawn for the parameters of case A. The crossing occurs for  $k\rho_H = 0.1$ , which translates into  $k\lambda_d \approx 0.7$ . Secondly, if the relative drift between the two beams increases, the two slopes  $\omega = kV_\alpha$  in Figure 1 grow further apart. As a result, the crossing point shifts toward ever smaller wavenumbers. For some limit, the crossing shifts where the branches have insignificant curvature and it disappears. The existence of a speed limit beyond which the instability vanishes stands in contrast to the classic two-stream instability mentioned at the beginning of this section. It has been pointed out in the context of auroral ion beams two decades ago [e.g., Bergmann and Lotko, 1986].

[11] An expression for the upper limit to the relative speed can be derived as follows. One rewrites the dielectric  $\epsilon$  in the frame of the  $O^+$  beam with  $U \equiv V_H - V_O$ , multiply it by  $k^2\lambda_d^2$ , introduces the notation  $r_H \equiv n_H/n_e$  and  $r_O \equiv n_O/n_e$  for the densities of  $H^+$  and  $O^+$  normalized to that of the electrons, and defines the parameter

$$\delta^3 \equiv \left( \frac{\omega_O}{\omega_H} \right)^2 = \frac{r_O}{r_H} \frac{M_H}{M_O}. \quad (5)$$

This yields

$$\bar{\epsilon} = 1 + k^2\lambda_d^2 - r_H C_{SH}^2 \left[ \frac{k^2}{(\omega - kU)^2} + \delta^3 \frac{k^2}{\omega^2} \right]. \quad (6)$$

It is clear that  $\bar{\epsilon}$ , considered as a function of the phase velocity  $\omega/k$ , has a local maximum comprised between two asymptotes where  $\bar{\epsilon}$  tends to  $-\infty$ . That maximum occurs for a phase velocity within the interval  $0 < \omega/k < U$  and has for value

$$\bar{\epsilon}_0 = 1 + k^2\lambda_d^2 - r_H(C_{SH}/U)^2(1 + \delta)^3. \quad (7)$$

Depending upon the value of the relative drift  $U$ , one has  $\bar{\epsilon}_0 \leq 0$ . Complex roots to  $\bar{\epsilon} = 0$ , hence instability, requires  $\bar{\epsilon}_0 < 0$ , hence  $U$  small compared to  $C_{SH}$ . For larger  $U$ , though,  $\bar{\epsilon}_0$  turns positive, hence the roots become real and the instability disappears. After minimizing  $\bar{\epsilon}_0$  with  $k\lambda_d \rightarrow 0$ , one obtains the limiting stability speed

$$U_L = C_{SH} \left[ r_H^{1/3} + (r_O/16)^{1/3} \right]^{3/2}. \quad (8)$$

The expression is equivalent to equation (1c) in Bergmann *et al.* [1988], save for  $k\lambda_d \rightarrow 0$  and for  $C_{SH}$  that has been redefined herein to include the effect of the plasma sheet ions, namely  $C_{SH} = (T_e/M_H)^{1/2}\Psi$ . To close this section, we note that the phase velocity of the unstable acoustic wave lies nearer to  $V_O$  than to  $V_H$  since the parameter  $\delta$  in (6) is smaller than

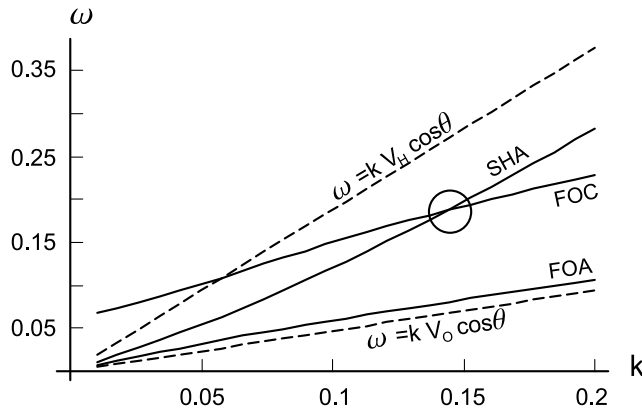


**Figure 2.** Schematic of the dispersion for oblique propagation ( $\cos\theta < 1$ ) and acoustic-cyclotron coupling. Doppler frequencies of the two beams,  $H^+$  and  $O^+$ , are indicated by dashed lines. The slow acoustic mode of the  $H^+$  beam (marked SHA) crosses the fast cyclotron mode of the  $O^+$  beam (marked FOC), leading to an instability. More details can be found in the text. Units:  $H^+$  gyrofrequency and gyroradius. Parameters in Table 1, Case B.

unity. For example, with the values in Table 1 case A we estimate the phase velocity to be 2.6, hence near to  $V_O$ . As we shall see later, this is important to allow for the trapping of the  $O^+$  ions in the acoustic wave.

## 2.2. Magnetic Effects and Two-Dimensional Geometry

[12] After taking into account magnetic and thermal effects, the pair of acoustic modes changes from equation (4) to

$$\omega(k_{\parallel}, k_{\perp}) = k_{\parallel} V_{\alpha} \pm k_{\parallel} C_{s\alpha} \left\{ \frac{(1 - r_{ps}) \Lambda_0(k_{\perp}^2 \rho_{\alpha}^2)}{1 + k^2 \lambda_d^2 + r_{\alpha} (T_e/T_{\alpha}) (1 - \Lambda_0(k_{\perp}^2 \rho_{\alpha}^2))} \right\}^{1/2} \quad (9)$$

where  $\alpha = H, O$  denotes the species with thermal spread  $v_{\alpha}$  and gyroradius  $\rho_{\alpha} \equiv v_{\alpha}/\Omega_{\alpha}$ . As usual for oblique wavevector, the modified Bessel function  $\Lambda_0(x) \equiv e^{-x} I_0(x)$  enters the expression. From mere inspection of the curly bracket in equation (9) one can see that increasing the perpendicular component of the wavenumber  $k_{\perp}$  reduces the phase velocity. Note that the coefficient  $T_e/T_{\alpha}$  in the denominator is a large number which more than offsets the density ratio  $r_{\alpha}$  for parameters in the auroral cavity (see Table 2). Still, equation (9) shows that the acoustic waves basically have a one-dimensional propagation along the magnetic field. As for the acoustic-acoustic mode coupling discussed in section 2.1 and the resulting instability, the same limit  $U_L$  defined by equation (8) applies for the relative drift  $V_H - V_O$ , irrespectively of the angle  $\theta$  between the wavevector and the magnetic field direction [Bergmann *et al.*, 1988]. That characteristic can easily be understood from equation (9) once it is realized that the term in the square bracket only decreases for  $\theta \neq 0$ . Even if the projection factor  $\cos\theta = k_{\parallel}/k$  can reduce the magnitude of the first term in (9) in case of a large value of  $V_{\alpha}$ , the same projection factor reduces the second term in proportion. Hence, if the two branches cannot intersect for  $\theta = 0$ , the same is a fortiori true for  $\theta > 0$ .

[13] The main change brought by the two-dimensional geometry is the possible propagation of oblique, short-wavelength cyclotron waves. To each ion beam one can associate a new pair of modes:

$$\omega(k_{\parallel}, k_{\perp}) = k_{\parallel} V_{\alpha} \pm \left[ \Omega_{\alpha}^2 + (1 - r_{ps}) \frac{k_{\perp}^2 C_{s\alpha}^2}{1 + k^2 \lambda_d^2} \right]^{1/2} \quad (10)$$

with  $\Omega_{\alpha}$  the cyclotron frequency of species  $\alpha$ . This enriches the possible couplings between the slow modes (either acoustic or cyclotron) of the faster, proton beam and the fast modes (either acoustic or cyclotron) of the slower oxygen beam. An important consequence is to circumvent the speed limit  $U_L$  defined by equation (8). Unlike for equation (9) the projection factor  $\cos\theta = k_{\parallel}/k$  here reduces only the slope of the Doppler term  $\omega = kV_{\alpha} \cos\theta$ . Thus one can offset too large a relative drift  $U$  by means of a factor  $\cos\theta < 1$ , whereby branches associated with the two beams can still intersect. Figure 2 shows the situation relevant to our case B, our so-called high-drift case (see Tables 1 and 2). The two dashed lines indicate the Doppler frequency of the beams. The slow acoustic mode (− sign in (9)) carried by the faster, hydrogen beam is shown by the solid line marked SHA. It crosses the line marked FOC, which displays the fast cyclotron mode (+ sign in (10)) carried by the oxygen beam. Meanwhile, the fast acoustic mode associated with the oxygen beam, which is marked FOA and plays an important role in case A, lies here very close to the Doppler frequency due to the small value of  $k_{\parallel}$ . Thus the acoustic-acoustic coupling in Figure 1 has been replaced by an acoustic-cyclotron coupling.

## 2.3. Transition Energy

[14] Since  $U_L$  in equation (8) relates to the relative speed between the two beam species and their individual speeds are in a definite ratio,  $V_H = 4V_O$ , one can define a transition energy  $E_T$  for the beams. Ion beams with a “drift energy” lower than  $E_T$  generate parallel, acoustic waves. Ion beams with a higher “drift energy” generate oblique, cyclotron waves. We find

$$E_T = T_e \Psi^2 (8/9) \left[ r_H^{1/3} + (r_O/16)^{1/3} \right]^3. \quad (11)$$

Basically, the transition energy is defined by the electron temperature. In addition, the ion composition plays a role. A mixture with a high proportion of oxygen ions rather than protons tends to decrease its value and so does a high proportion of plasma sheet protons, which diminishes the factor  $\Psi$ . For illustration, the parameters in Table 2 yield  $E_T = 1016$  eV. In the simulation runs to be presented in section 3, the cold ion beams are injected with a drift energy  $K_d = 835$  eV for case A and  $K_d = 2110$  eV for case B, namely below and above  $E_T$ , where Figures 1 and 2 apply, respectively.

## 3. PIC Simulations of $H^+ - O^+$ Instabilities

[15] In order to study how  $H^+ - O^+$  two-stream instabilities develop and evolve into the nonlinear stage, we perform a series of specially designed PIC simulations. We wish to examine their development as a spatially

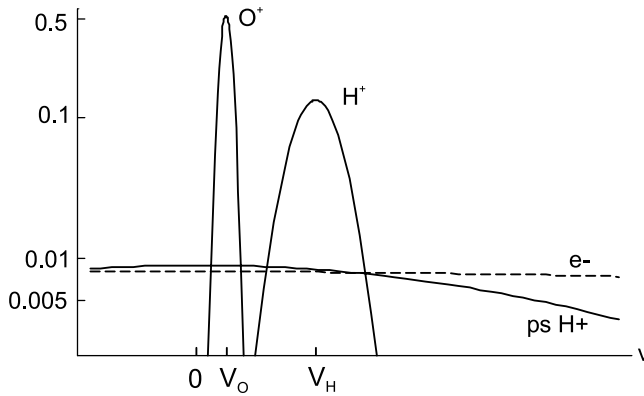


**Figure 3.** Schematic of the distributions for the four species used in the simulations. Electrons (dashed line marked  $e^-$ ) and plasma sheet protons (solid line marked  $ps\ H^+$ ) have large thermal velocities and no average drift. The two beams of ionospheric origin,  $H^+$  and  $O^+$ , have a drift speed larger than their thermal spread. Their drift energy is the same,  $V_H = 4V_O$ .

inhomogeneous problem, in contrast to previous PIC simulations, which have considered their development as a homogeneous, temporal problem [Roth *et al.*, 1989; Crumley *et al.*, 2001]. An essential aspect of the auroral environment of these instabilities, we believe, is the constant injection of hydrogen and oxygen ions at the bottom of the cavity. The strong double layer which presumably accelerates these ions from the ionosphere into the cavity was recently simulated by means of a Vlasov code [Main *et al.*, 2006]. The present PIC simulation box does not include the double layer. Rather, our model describes the evolution of an open, magnetized subsystem located in the cavity above the accelerating double layer. The model is oriented parallel to the magnetic field lines in such a way that the left boundary of the simulation box corresponds to the low-altitude end of the cavity. Thus beams of protons and oxygens with equal energy are injected along the magnetic field at the left boundary. One follows the particle dynamics of all species, including electrons and plasma sheet protons. The distribution functions of the four species is shown schematically in Figure 3. Electrons and plasma sheet protons have large thermal velocities yet no average drift, whereas the two ion beams of ionospheric origin have a net drift larger than their thermal spread. Fresh particles sampled from these distributions continuously enter the simulation box while exiting particles are removed from the system.

[16] Even though the auroral plasma is strongly magnetized, a challenge for these PIC simulations is to reach oxygen cyclotron times with steps small enough to resolve the electron motion. For that purpose we assume two alterations to the electron dynamics. First, a fake mass ratio of  $m/M_H = 0.01$  is used. Secondly, the electrons are considered as infinitely magnetized: their motion is restricted to occur along the field lines, which seems appropriate in view of the large  $\Omega_e/\omega_e$  ratio prevalent in the cavity and the fact that we focus on relatively low-frequency waves. In addition, the computationally intensive 2D3V simulation runs

are performed by successive installments of typically 4000 steps, or  $40/\pi$  proton cyclotron periods, for a time step  $\Delta t = 0.02\ \Omega_H^{-1} = 0.149\ \omega_e^{-1}$ .

### 3.1. Case A: Low Drift

[17] Here we consider ion beams that have a drift energy below the transition energy  $E_T$ . Therefore, following the analysis made in section 2, parallel acoustic waves are expected to grow unstable. Entering the parameters of case A (shown in Tables 1 and 2) into a numerical dispersion code yields unstable acoustic waves having wavenumbers in the range  $0.007 < k\rho_H < 0.14$ , with a peak in the growth rate for  $k\rho_H \approx 0.08$ . At this peak the growth rate reaches  $\gamma = 0.03\ \Omega_H$  and the real frequency in the simulation frame is of order  $\omega \approx 0.2\ \Omega_H$ . The group velocity reads  $2.5\ v_H$ , hence the convective growth length is on the order of  $80\ \rho_H$ .

#### 3.1.1. 1D1V Simulations

[18] First we present results of a 1D1V PIC simulation of the instability, the one dimension being the direction of the magnetic field as well as that of the drift. A long grid of 512 cells that spans 2048 proton gyroradii (or 150 Km) is used and the system is simulated for times as long as 80 proton cyclotron periods (or 5 oxygen cyclotron periods). We typically employ 2000 to 5000 macroparticles per cell to describe the various populations. The large number density enables us to limit the noise at the open boundaries by injecting a substantial number of particles for each time step. For example, in the 1D run to be shown in Figure 4 we inject an average of 272.3 macroelectrons into the left boundary cell per time step. By contrast, in the corresponding 2D3V simulations, which will be presented in section 3.1.3, we inject only 8 macroelectrons per cell albeit among the 128 cells that constitute the left boundary. Besides the reduced noise, the 1D simulations have several practical advantages over the 2D simulations. They are more flexible to use, which makes them more convenient to explore the role of different parameters. They allow for a longer simulation box and the system can be simulated for a longer period of time.

[19] Figure 4 displays results from early times. The graph on top shows three successive power spectra in  $k$  which evidence the growth of an instability. The electrostatic field grows on a timescale of order  $40\ \Omega_H^{-1}$  over a range of wavenumbers which peaks for  $k \lesssim 0.1$ . Also, we recorded the time series of the electric field as seen by fixed probes. The resulting frequency spectrum (not shown) exhibits enhanced power about  $\omega \approx 0.2\ \Omega_H$ . Thus unstable wave-number, frequency, and growth rate match well our expectations from the numerical dispersion code and from Figure 1.

[20] At  $t = 160\ \Omega_H^{-1}$  the first signs of ion trapping in the electrostatic potential of the acoustic wave become visible. A snapshot of the proton and oxygen  $[x, v_x]$  phase spaces, Figure 4 (bottom), shows that about  $x \sim 400\ \rho_H$  the wave field has already gained enough amplitude to trap some of the protons. They lose momentum while the  $O^+$  ions are slightly accelerated. We note that the inhomogeneous wave field, reflected here in the inhomogeneous phase space, is typical of the open-boundary setting of our code. The continuous injection of unstable beams at the left boundary enhances the wave field in the proximity of this boundary. The injection's influence propagates at the group velocity and by this time covers a distance of  $2.5 \times 160 = 400$ . Five convective growth lengths is apparently what it takes to

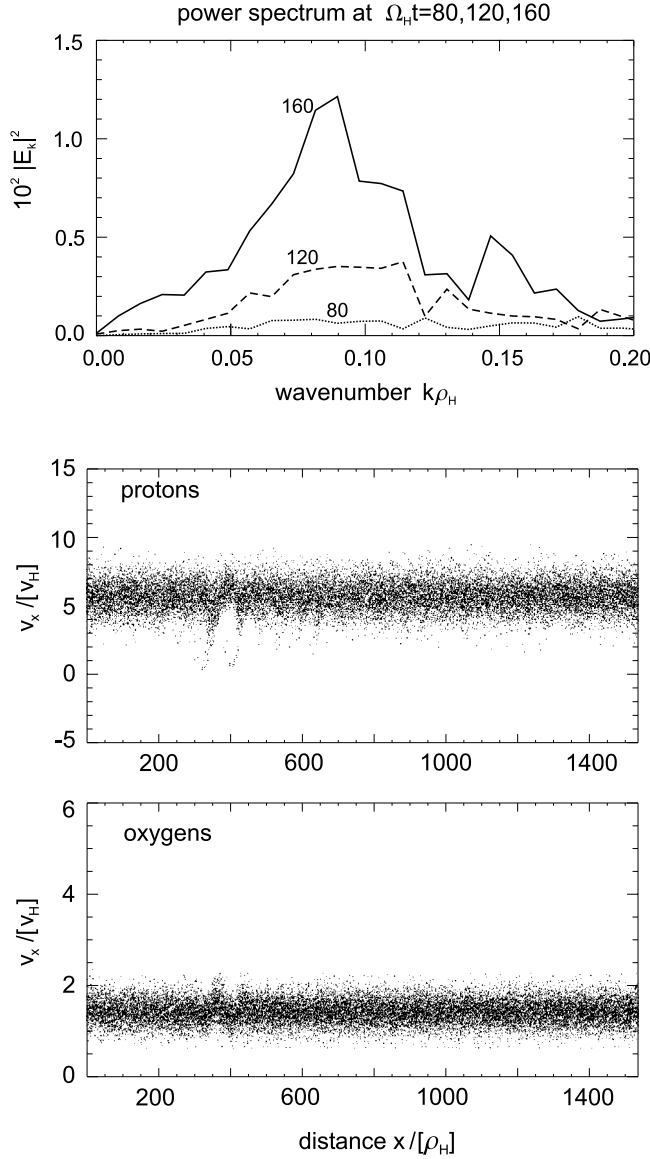


**Figure 4.** Simulation results for the low-drift case at early times. (top) Three successive power spectra that evidence growth on a  $40 \Omega_H^{-1}$  timescale (dotted, dashed, and solid lines labeled with  $\Omega_H t$ ). (middle and bottom) Snapshot of  $H^+$  and  $O^+$  phase spaces at  $\Omega_H t = 160$ . First signs of proton trapping visible about  $x/\rho_H \sim 400$ . More details can be found in the text. Parameters in Table 1, Case A.

bring the wave field from noise to a weakly nonlinear level where the trapping begins.

[21] As the instability further develops, full vortices of trapped protons form and drift toward the right (namely toward higher altitudes) at a speed  $\sim 2.5 v_H$ . Meanwhile, new proton vortices begin forming about  $x \sim 400 \rho_H$ . This is illustrated in Figure 5. The first and second panels display a snapshot of the proton and oxygen  $[x, v_x]$  phase spaces at  $t = 260 \Omega_H^{-1}$ . The thirds and fourth panels display the same phase spaces later at  $t = 300 \Omega_H^{-1}$ . Distance is indicated in our normalized unit of proton gyroradius as well as in Debye length for convenience. The scale of a vortex is seen

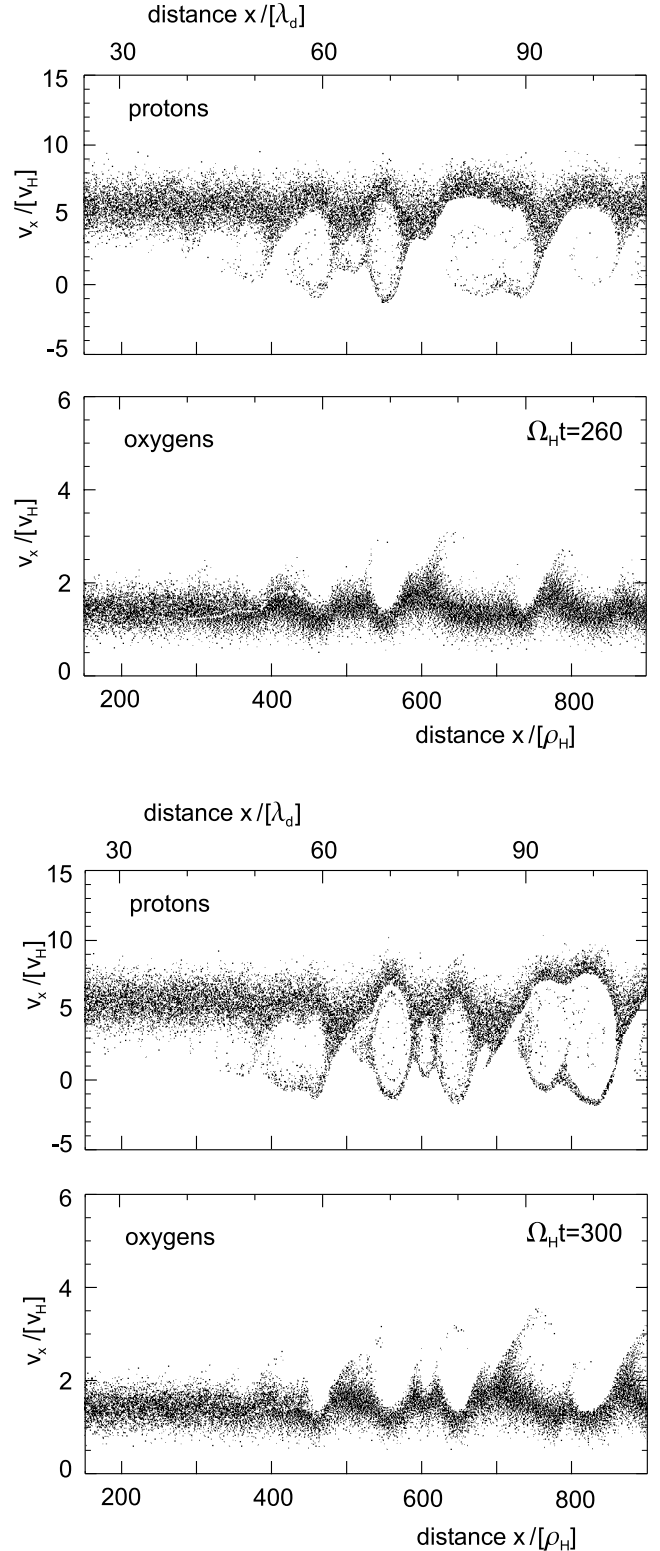


**Figure 5.** Two successive snapshots of  $H^+$  and  $O^+$  phase spaces at times  $t = 260, 300 \Omega_H^{-1}$ . Vortices of trapped protons form about  $x/\rho_H \sim 400$  and drift toward increasing  $x$ . Oxygen ions, though evidencing strong acceleration, take longer to build vortices. More details can be found in the text. Spatial scales marked in both proton gyroradius and Debye length. Parameters in Table 1, Case A.

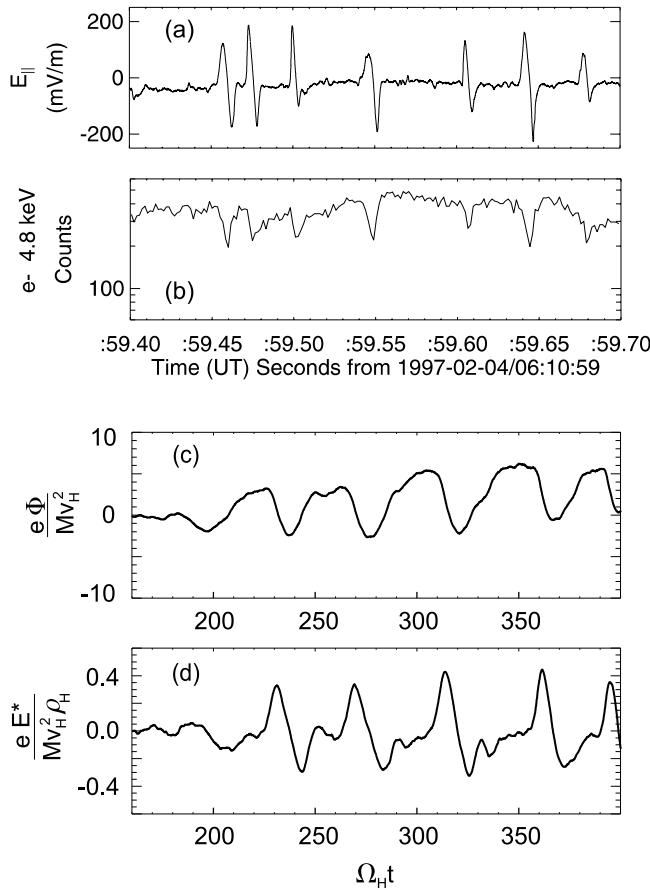


**Figure 6.** (a) and (b) Example of ISWs measured by FAST. Figure 6a shows the characteristic bipolar electric signal parallel to the magnetic field. Each bipolar spike is consistent with a negative potential hump moving upwards. Accordingly, Figure 6b shows the electron count in a high-energy channel dips. (c) and (d). From the simulation shown in Figure 5. A probe located at  $x = 500 \rho_H$  record potential and electric field as proton holes pass by. Figure 6c shows the potential in normalized units (see Table 3). Figure 6d shows the electric field in normalized units. Note that its sign has been redefined so that  $E^* > 0$  points downwards, or opposite to the beam direction, following the FAST convention. More details can be found in the text.

to be less than ten Debye lengths. In the first and third panels, notice a small vortex flanked by two larger ones that is visible at  $x \sim 500 \rho_H$ . The same group can be identified later at  $x \sim 600 \rho_H$ , its leftmost vortex being now fully formed. Meanwhile, a new proton vortex is appearing at  $x \sim 400 \rho_H$ .

[22] The oxygen phase spaces in Figure 5 evidence strong acceleration of  $O^+$  by the acoustic wave field. However, no closed loops appear in this portion of phase space, even at later times. The  $O^+$  trapping period being four times longer than that of  $H^+$ , well formed proton vortices and their associated potential wells drift away in the time it takes an oxygen ion to bounce back and forth. Using a peak electric field  $|E| = 0.4$  and  $k\rho_H = 0.08$ , we estimate the trapping frequency of an  $O^+$  ion to be  $\omega_b = 0.045 \Omega_H$ , which

yields a bounce period of  $140 \Omega_H^{-1}$ . Note that the trapping velocity is  $v_{tra} = 2\omega_b/k = 1.1 v_H$ . It is therefore clear, looking at the oxygen panels in Figure 5, that a potential well moving with speed  $2.5 v_H$  can reach deeply into the oxygen distribution. Further downstream in the simulation box we indeed observe closed loops which evidence the trapping of  $O^+$ . Still, we never see as nicely formed  $O^+$  vortices as for  $H^+$ , which we attribute to the following. The proton vortices do evolve as they propagate and collide with each other. The time scale for these changes being not long compared to the bounce period of an  $O^+$  ion, no “equilibrium” with the oxygens’ dynamics can be established.

### 3.1.2. Proton Holes and Ion Solitary Waves

[23] As mentioned in the Introduction, ion solitary waves (ISWs) are characterized by a negative potential hump accompanied with a localized density depletion. They appear to be associated with the upflowing ion beams of upward current regions [Bounds *et al.*, 1999; Dombek *et al.*, 2001; McFadden *et al.*, 2003]. Figures 6a and 6b displays an example of ISWs measured by the FAST satellite. In Figure 6a, we show the characteristic bipolar electric signal where each positive spike is followed in time by a negative spike. Here a positive electric field points earthward, namely opposite to the direction of the beams. The signal is thus consistent with a negative potential hump moving upward. That is confirmed in Figure 6b, which indicates the particle count in a high-energy channel (4.8 keV) of the electron instrument. Concomitant with each bipolar signal the electron count dips as can be expected from the retarding effect of a negative potential hump on the fast electrons.

[24] The simulation shown in Figure 5 had probes set up at various positions in the box to record the electrostatic potential and the electric field. The probes, emulating the role of a spacecraft instrument, record their time variations while the proton vortices drift by. A low-pass filter is used to eliminate fast variations on the order of the electron time scale. The recordings of one such probe located at  $x = 500 \rho_H$  are shown in Figures 6c and 6d. As the proton holes pass by, potential dips and bipolar electric pulses are recorded. Note that to facilitate the comparison with the FAST sample of ISWs, where  $x > 0$  points opposite to the direction of the beam propagation, we have here redefined the electric field as  $E^* = +\partial\phi/\partial x$ . Using Table 3 for conversion to physical values, one finds that the bipolar spikes present in the simulation have a field up to 280 mV/m. This is similar to the values observed by FAST for ion solitary waves [McFadden *et al.*, 2003]. Albeit a bit larger than the 200 mV/m spikes of the sample shown in Figure 6a, it is less than the 500 mV/m reported for the most intense ISWs. Another characteristic of the electric waveform that can be compared is the time delay  $\tau$  measured as the lag between two opposite electric spikes. In Figure 6d  $\tau$  is about  $12 \Omega_H^{-1} = 12$  ms, namely twice larger than  $\tau$  in Figure 6a. The ion beams used in the simulation are somewhat slow, which might partially explain the longer time delay. Nevertheless, 12 ms fits in the 4 to 15 ms range of  $\tau$  values reported by FAST for ISWs [McFadden *et al.*, 2003]. The potential throughs in Figure 6c correspond to 350 V using Table 3 for conversion to physical values. That value is at the low end of the estimates reported by [McFadden *et al.*, 2003] which range from 250 V to

**Table 3.** Correspondence Between Physical and Normalized Units

Units	Normalized	Physical
Length	$\rho_H$	73 m
Time	$\Omega_H^{-1}$	1 ms
Velocity	$v_H$	71 km/s
Electric field	$\Omega_H^2 \rho_H M_H/e$	700 mV/m
Potential	$v_H^2 M_H/e$	52 V

900 V. Note that the potential dip signals that a density depletion accompanies each proton vortex in agreement with the rarefactive aspect of ISWs. Assuming Boltzman's law for the electrons, one finds  $\delta n/n_0 = \Phi (M_H v_H^2 / m v_e^2) \sim -0.2$ , i.e., a 20% depletion. In summary, the comparison suggests that the observed ISWs are a signature of proton holes generated by the  $H^+ - O^+$  two-stream instability in parallel propagation.

### 3.1.3. 2D3V Simulations, Case A: Low Drift

[25] Other simulations of the same acoustic instability were performed on a two-dimensional box in order to verify its parallel character. We report here on a simulation with a grid that resolves  $400 \times 128$  cells and spans  $1200 \times 384$  ionospheric proton gyroradii ( $88 \times 28$  Kms). The electrostatic field has two components,  $E_x$  parallel to the magnetic field and  $E_y$  perpendicular to it, while the particles have three velocity components,  $v_x$ ,  $v_y$ , and  $v_z$ . The boundary conditions are open in the  $x$  direction, namely parallel to the magnetic field, and periodic in the  $y$  direction. We typically employ  $24 \cdot 10^6$  macroparticles for the electrons,  $12 \cdot 10^6$

macroparticles for the protons as well as for the oxygens, and  $8 \cdot 10^6$  macroparticles for the plasma sheet protons. There are thus a total of over  $10^3$  macroparticles per cell and the computational effort is distributed over eight processors. The parameters are again those of Table 1 case A.

[26] Figure 7 displays the electric field at time  $t = 180 \Omega_H^{-1}$ . A low-pass filter has been used to eliminate the high-frequency part of the field that varies on the electron timescale. In Figure 7 (top) one can see that the parallel component  $E_x$  exhibits ridges which run roughly in the  $y$ -direction, i.e., perpendicularly to the magnetic field. Meanwhile, Figure 7 (bottom), which shows the perpendicular component  $E_y$ , exhibits much less intense activity. Although not lined up in a very orderly manner, the ridges evidence acoustic waves propagating parallel to the magnetic field. The waves, which have wavelengths consistent with the 1D simulation of section 3.1.1, are well developed with peaks in the electric field typically attaining  $|E_x| = 0.2$  by the time shown. Later on, they reach up to  $|E_x| = 0.4$  (280 mV/m) like the bipolar electric spikes shown in Figure 6d. At the left of the simulation box we notice a region which seems devoid of activity. That reflects our open-boundary setting: the unstable acoustic waves, while being amplified, are carried rightward by the beams, so that they reach a significant level only away from the injection boundary.

[27] As in the 1D simulation presented in section 3.1.1, trapping is visible in the proton and oxygen  $[x, v_x]$  phase spaces. By  $t = 180 \Omega_H^{-1}$  proton vortices are formed, yet closed loops of oxygens appear only later at  $t = 280 \Omega_H^{-1}$ . That the parallel component  $E_x$  of the electric field domi-

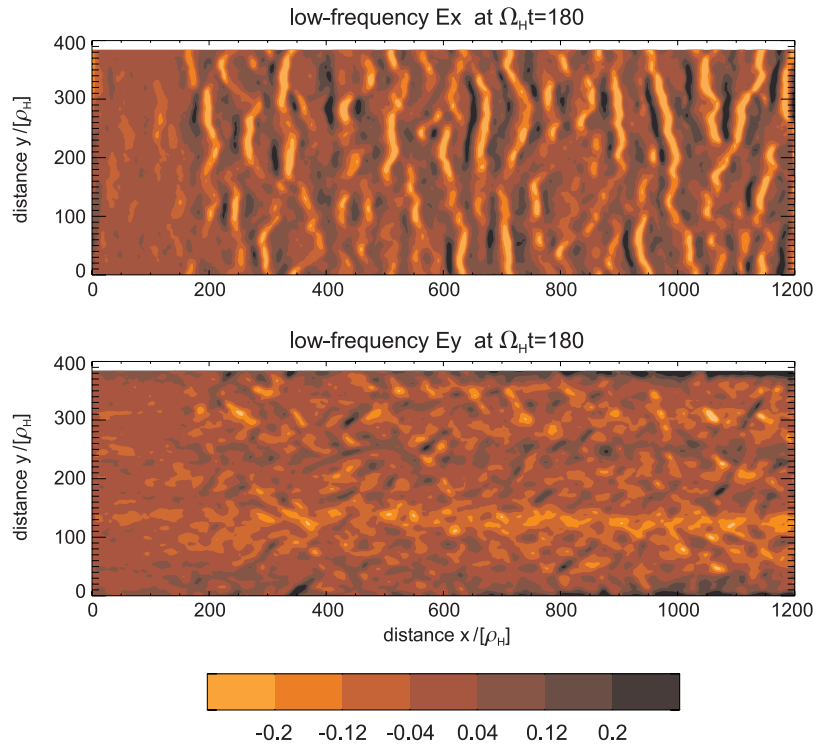


**Figure 7.** 2D3V simulation of the low-drift case. Most of the electric field activity is in the parallel component  $E_x$ . Note the ridges that run roughly in the  $y$ -direction. They evidence acoustic waves propagating parallel to the magnetic field with wavelengths consistent with the 1D simulation. Parameters in Table 1, Case A.

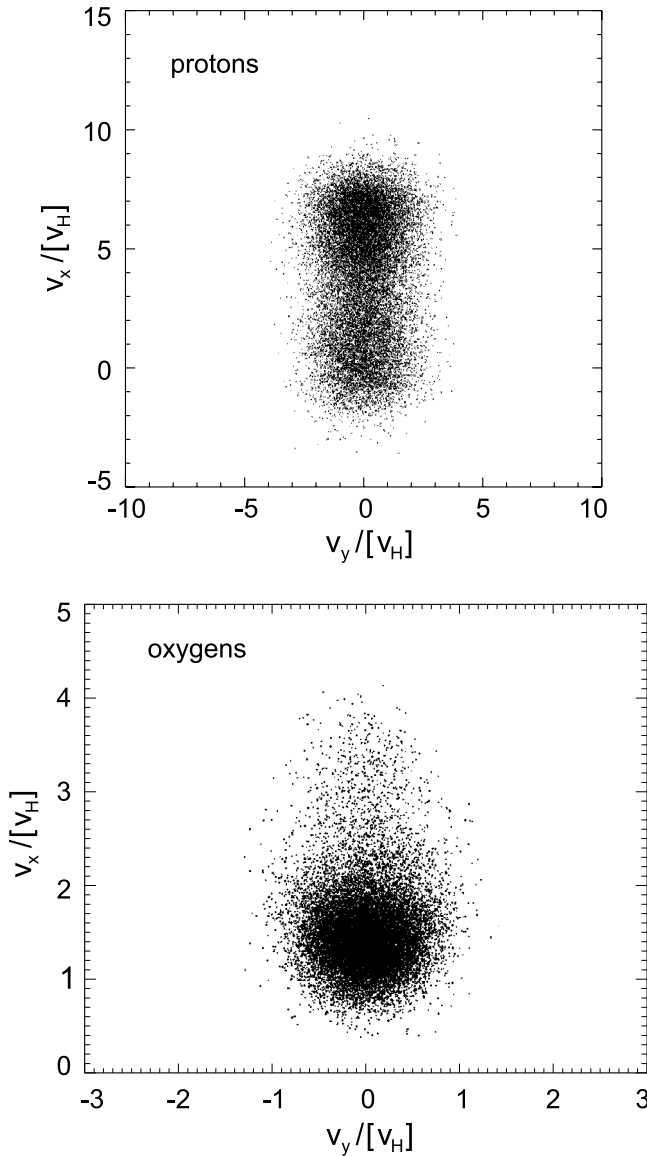


**Figure 8.**  $[v_x, v_y]$  phase spaces for  $H^+$  and  $O^+$  in the low-drift case. Same run as in Figure 7. Particles with positions  $500 < x/\rho_H < 1050$  at late time  $\Omega_H t = 280$  are included. Most of the diffusion happens in  $v_x$ , namely, along the magnetic field. Parameters in Table 1, Case A.

notes the interaction between the  $H^+$  and  $O^+$  beams is further confirmed in Figure 8. Here we display the proton and oxygen  $[v_y, v_x]$  phase spaces averaged over the section  $500 < x < 1050$  of the simulation box. Whereas the initial/injected proton beam had a drift  $V_H = 5.7$  and thermal velocity  $v_H = 1$ , the protons now have parallel velocities  $v_x$  spreading from  $+8.5$  down to  $-2$ . Their perpendicular velocities  $v_y$  spread from  $-2.5$  to  $+2.5$ , which is similar to initially. Whereas the initial/injected oxygen beam had a drift  $V_O = 1.4$  and thermal velocity  $v_O = 0.25$ , the oxygen ions now have a parallel velocity  $v_x$  spreading from  $+0.6$  up to  $+3.8$ . Their perpendicular velocities show little heating since  $v_y$  spread from  $-1.0$  to  $+1.0$ , just a little more than the initial  $[-0.7, +0.7]$ . Table 4 summarizes the simulation results in

terms of energy exchanges between  $H^+$  and  $O^+$ . For each species we have divided the parallel energy into a “drift energy”,  $K_d \equiv 0.5M \langle v_x \rangle^2$ , and a parallel spread energy,  $K_{\parallel} \equiv 0.5M \langle v_x^2 \rangle - K_d$ . Also, we have defined a perpendicular spread energy,  $K_{\perp} \equiv 0.5M \langle v_y^2 + v_z^2 \rangle$ . Table 4 indicates the values at the end of the run,  $t = 280 \Omega_H^{-1}$ , as well as the initial/injected values in parenthesis. One notices a big drop in the drift energy of the protons accompanied by an increase in their parallel spread energy. Meanwhile, the oxygens experience an increase in their drift energy and in their parallel spread energy, as well as a more modest increase in their perpendicular spread energy. One thus concludes that the parallel component  $E_x$  of the electric field dominates the instability.

### 3.2. Case B: High Drift

#### 3.2.1. 1D1V Simulations

[28] When the drift energy of the injected beams is larger than the transition energy  $E_T$ , which is defined by equation (11), PIC simulations performed with the 1D1V code evidence no instability. As compared to the low-drift case A, the power spectrum remains at all times substantially lower and displays no marked peak, while the phase spaces show no sign of ion trapping. This therefore confirms the expectation from the dispersion study that the acoustic instability disappears. On the other hand, as we noted when discussing Figure 2, a coupling between the two ion beams is possible that involves an oblique, oxygen cyclotron mode.

#### 3.2.2. 2D3V Simulations, Case B

[29] We now present the results of a simulation performed on a two-dimensional box which allows for the propagation of oblique cyclotron waves. The settings are the same as described in section 3.1.3 except for the injected ion beams whose parameters are given in Table 1 case B. The grid includes  $400 \times 128$  cells, which in terms of initial gyroradii means that the grid spans  $1200 \times 384 \rho_H$ , or  $300 \times 96 \rho_O$  ( $88 \times 28$  Km). One employs a total of over  $10^3$  macro-particles per cell and the computational effort is distributed over eight processors. A full simulation run uses close to 100 hours of CPU on an IBM P655.

[30] Until  $t \sim 200 \Omega_H^{-1}$  no sign of low-frequency wave activity is visible, which is not surprising since the fast-growing acoustic instability is absent. On the other hand, about  $t \sim 240 \Omega_H^{-1}$  the perpendicular component of the electric field  $E_y$  begins to exhibit some wave pattern. As previously, we use a low-pass filter to eliminate the part of the field that varies on the electron timescale. At  $t = 240 \Omega_H^{-1}$  the perpendicular field reaches typical values  $|E_y| \lesssim 0.1$ . An inspection of the  $[x, v_x]$  phase spaces indicates that a small fraction of the protons have been decelerated while the oxygen distribution seems unchanged. Later, at  $t \sim 320 \Omega_H^{-1}$  the wave patterns in  $E_y$  are well developed with  $|E_y| \lesssim 0.3$  (200 mV/m). The parallel component remains much

**Table 4.** Kinetic Energies in Case A<sup>a</sup>

Species	$K_{\perp}$	$K_{\parallel}$	$K_d$
Proton	1.1 (1.0)	3.6 (0.5)	8.3 (16.)
Oxygen	1.9 (1.0)	1.5 (0.5)	18 (16.)

<sup>a</sup>Initial/injected values shown in parenthesis.

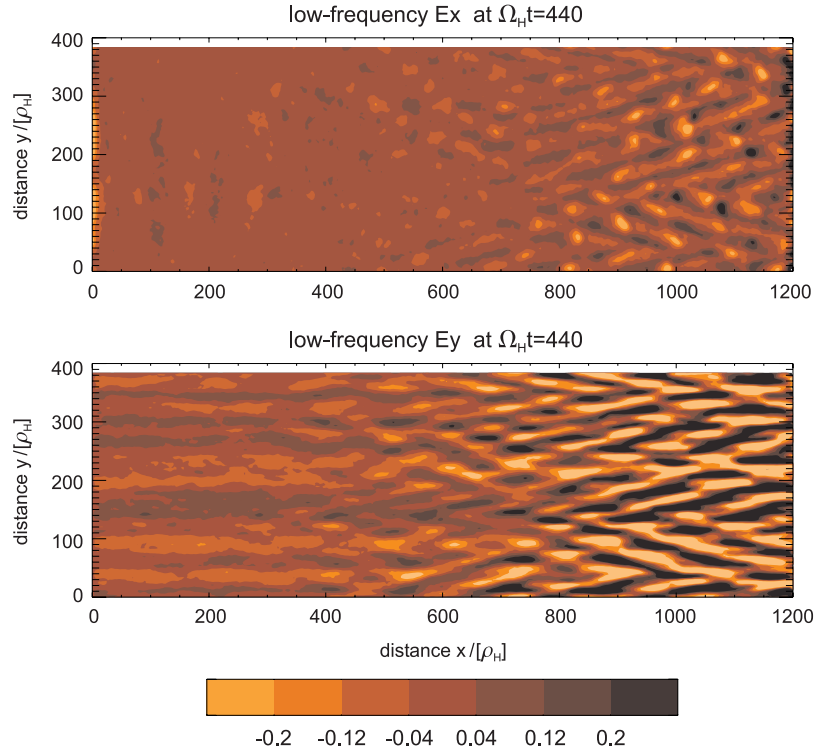


**Figure 9.** 2D3V simulation of the high-drift case. Most electric field activity is in the perpendicular component  $E_y$ , by contrast to the low-drift case shown in Figure 7. Note the herringbone pattern formed by obliquely propagating cyclotron waves and the considerable stand-off distance from the injection boundary, which is due to their large convective growth length. Parameters in Table 1, Case B.

smaller,  $|E_x| \lesssim 0.05$ . A power spectrum of the perpendicular field indicates preferred perpendicular wavenumbers for  $k_y \rho_H \sim 0.15$ , namely  $k_y \rho_O \sim 0.6$ , which is a good indication that indeed oxygen cyclotron waves are growing. A plot of the low-frequency electric field is shown in Figure 9 in the same format as used in Figure 7. Contrasting with Figure 7 though, the main activity appears in Figure 9 (bottom), which displays the perpendicular component. Note the herringbone pattern formed by the obliquely propagating waves. The same pattern, albeit fainter, is visible in Figure 9 (top) showing  $E_x$ . We estimate the propagation angle to  $77^\circ \pm 2^\circ$ , which leads to a parallel wavelength of  $180 \rho_H$ . Note also the large standoff distance between the injection boundary and the edge of the wave activity.

[31] Since the obliquely propagating waves crisscross, the herringbone pattern is constantly changing in its details. One needs to take snapshots at time intervals  $\Omega_H \tau = 5$  to be able to identify the propagating wavefronts. In Figure 10, we zoom in on a quarter of the simulation box and examine the propagation. One feature, underscored by a blue line, moves toward increasing  $x$  and  $y$ . It corresponds to a wavefront with propagation vector  $\mathbf{k} = [k_x > 0, k_y > 0]$ . Another feature, underscored by a green line, moves toward increasing  $x$  yet decreasing  $y$ . It corresponds to a wavefront with propagation vector  $\mathbf{k} = [k_x > 0, k_y < 0]$ . After inspecting several such features, we could determine that the parallel phase velocity, denoted by  $\zeta_{\parallel} \equiv \omega/k_{\parallel}$ , has an average value  $\zeta_{\parallel} = 5.8 v_H$  with variations from 4 to 7. Now returning to Figure 2, one can roughly predict the phase velocity of the

unstable waves to be  $1.3 v_H$ , which with a  $77^\circ$  angle results in exactly the same parallel velocity of  $5.8 v_H$ . Thus the herringbone pattern is indeed formed by the obliquely propagating oxygen cyclotron waves that are destabilized by the ion two-stream instability.

[32] The cyclotron waves have a frequency  $\omega \sim 0.2 \Omega_H$  and a wavelength  $\lambda \sim 10 \rho_O$ . Due to their small growth rate they have a larger convective growth length than the acoustic waves in Figure 7. Hence the larger standoff distance from the injection boundary noticeable in Figure 9. Nevertheless, given enough time and a long enough box, they can reach a substantial level. At the late time shown in Figure 9,  $t = 440 \Omega_H^{-1}$ , the waves have saturated and peaks in the perpendicular electric field reach  $|E_y| = 0.4$ , similarly to the parallel component for the low-drift case we presented in section 3.1. Though smaller, the parallel component here is substantial with peaks reaching  $|E_x| = 0.1$  (or 70 mV/m).

[33] Let us consider the electrostatic potential of an oblique cyclotron wave as seen by an ion. If one assumes the usual, unperturbed, helical trajectories  $x = x_o + v_x \tau$ ,  $y = y_o + \rho_\alpha [\sin(\Omega_\alpha \tau + \vartheta) - \sin(\vartheta)]$  for the ion  $\alpha$ , and writes  $\zeta_{\parallel}$  for the parallel phase velocity of the wave, one obtains

$$\begin{aligned} \phi(\tau) = & \Phi \exp(i\varphi) \exp\left[ik_x(v_x - \zeta_{\parallel})\tau\right] \\ & \cdot \sum_{n=-\infty}^{+\infty} \sum_{m=-\infty}^{+\infty} J_n(k_y \rho_\alpha) J_m(k_y \rho_\alpha) \\ & \cdot \exp[in\Omega_\alpha \tau + i(n-m)\vartheta] \end{aligned} \quad (12)$$

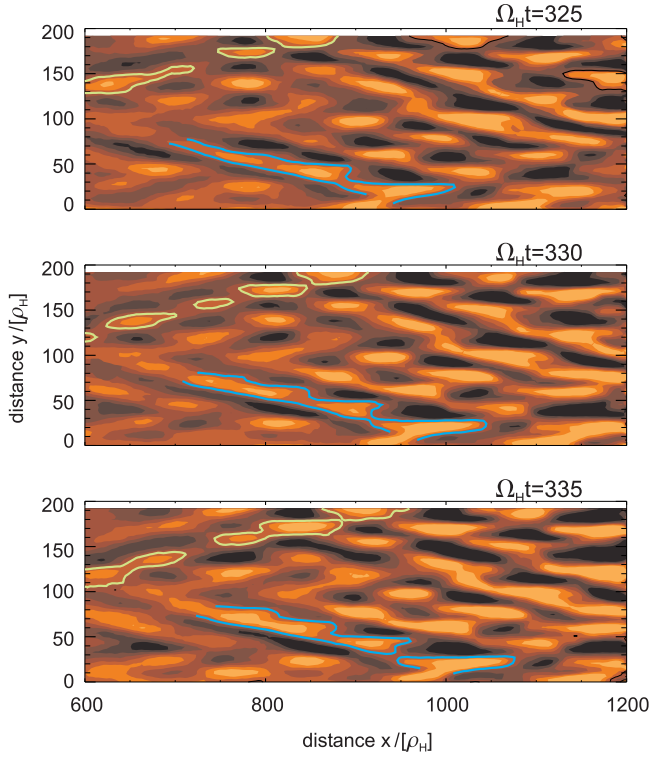


**Figure 10.** 2D3V simulation of the high-drift case. Zoomed-in view to examine the propagation of wavefronts. The pattern delineated by a blue (green) line moves toward increasing  $x$  and increasing  $y$  (decreasing  $y$ ). More details can be found in the text.

where  $\varphi$  includes the ion's initial position and the wave's initial phase. The first line deals with the effect of the parallel component  $E_x$  whereas the second and third lines deal with that of the perpendicular component  $E_y$ . For the protons ( $\alpha = H^+$ ) the double sums of Bessel functions simplifies considerably since their gyroradius is much smaller than the perpendicular wavelength. One has  $k_y \rho_H = 0.15$  and the term  $n = m = 0$  alone survives. The protons are considered as magnetized and effect a one-dimensional motion. On assuming a typical parallel wavenumber  $k_x \rho_H = 0.035$ , we evaluate their trapping frequency as  $\omega_b = 0.06 \Omega_H$  and their trapping velocity as  $v_{tra} = 2\omega_b/k_x = 3.4 v_H$ . The velocity difference  $\Delta v = |v_x - \zeta_{||}|$  in the resonance term on the first line of equation (12) may be evaluated by replacing  $v_x$  by  $V_H = 9 v_H$  and by recalling the estimate of the parallel phase velocity  $\zeta_{||} = 5.8 v_H$ . As  $\Delta v = 3.2 v_H$  is comparable to the trapping velocity, the field is strong enough to trap the protons. However, when inspecting the  $[x, v_x]$  phase space for evidence of trapping, one must consider narrow strips restricted in  $y$  due to the herringbone wave pattern. If one selects protons within strips of width  $\Delta y \lesssim \lambda_{\perp}/2 \approx 20 \rho_H$ , the phase space plots show indeed vortices of trapped particles. The vortices appear centered about  $5-7 v_H$ , which confirms our previous estimate of  $\zeta_{||}$ . They have a typical diameter of  $8 v_H$ , which is consistent with the trapping velocity evaluated above.

[34] A major difference, as compared to the low-drift case, is that the oxygen ions are not trapped. We now apply

equation (12) to the latter ( $\alpha = O^+$ ) and assess the velocity difference  $\Delta v = |v_x - \zeta_{||}|$  in the resonance term on the first line. Replacing  $v_x$  by  $V_O = 2.25 v_H$  and  $\zeta_{||}$  by  $5.8 v_H$ , one obtains  $\Delta v = 3.55 v_H$ . Yet for  $O^+$ , the trapping frequency and trapping velocity read  $\omega_b = 0.015 \Omega_H$  and  $v_{tra} = 0.86 v_H$ , respectively, because of the larger mass. As  $\Delta v \gg v_{tra}$ , the parallel component of the field is not strong enough to trap the oxygen ions. On the other hand, one has  $k_y \rho_O = 0.6$ , whereby the  $n \neq 0$  Bessel functions are important. In fact, the combination  $V_O - \zeta_{||} + 2\Omega_O/k_x = 0.03 v_H$  is close to zero. Because of that the oxygen ions strongly feel the  $E_y$  component of the wave electric field and are energized perpendicularly.

[35] A further confirmation that oxygen cyclotron waves and their accompanying perpendicular electric field play a

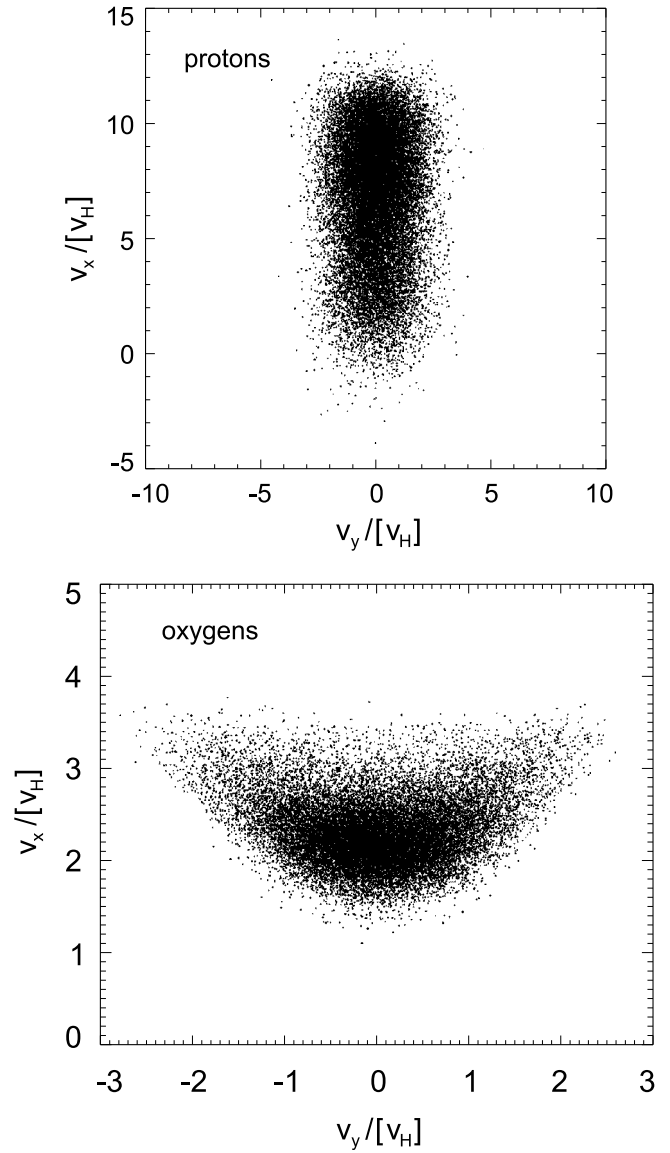


**Figure 11.**  $[v_x, v_y]$  phase spaces for  $H^+$  and  $O^+$  in the high-drift case. Oxygens form a drifting conic while the protons, which are magnetized on a  $O^+$  cyclotron timescale, diffuse mainly in the parallel direction. Parameters in Table 1, Case B.

**Table 5.** Kinetic Energies in Case B<sup>a</sup>

Species	$K_{\perp}$	$K_{\parallel}$	$K_d$
Proton	1.1 (1.0)	3.3 (0.5)	26.4 (40.5)
Oxygen	6.8 (1.0)	1.1 (0.5)	44.5 (40.5)

<sup>a</sup>Initial/injected values shown in parenthesis.

major role in the simulation is provided by Figure 11. Here we show the proton and oxygen [ $v_y$ ,  $v_x$ ] phase spaces averaged over the section  $900 < x/\rho_H < 1200$ , where the waves are the most intense. The protons, which are magnetized on an oxygen cyclotron timescale, diffuse in the parallel direction mainly. On the other hand, the oxygen ions respond to the perpendicular electric field and heat significantly in the perpendicular direction. Whereas the perpendicular velocities of the initial/injected  $O^+$  beam were confined between  $[-0.7, +0.7]$ , the oxygen ions now have velocities which spread from  $v_y = -2.4$  to  $v_y = +2.4$ . Meanwhile, their mean drift parallel to the magnetic field has modestly increased from  $V_O = 2.25$  to  $V_O = 2.36$ . The oxygens form a “drifting conic”. Table 5 summarizes the simulation results regarding the energy exchanges between  $H^+$  and  $O^+$ . It indicates values at the end of the run,  $t = 440 \Omega_H^{-1}$ , as well as, in parenthesis, the initial/injected values. Note the large drop in the drift energy of the protons from  $K_d = 40.5$  to  $K_d = 26.4$ , and the large increase in the perpendicular spread energy of the oxygens from  $K_{\perp} = 1.0$  to  $K_{\perp} = 6.8$ .

#### 4. Summary and Discussion

[36] We have investigated the interaction between  $H^+$  and  $O^+$  beams in the auroral acceleration cavity by means of 1D and 2D PIC codes. The simulation model has its main axis oriented parallel to the magnetic field lines and represents an open system where protons and oxygen ions are constantly injected with the same energy at the lower boundary, emulating the ion influx from the cavity’s bottom. Besides the ion beams, the simulations include a population of plasma sheet protons and of hot electrons. The results evidence two regimes depending upon the drift energy  $K_d$  of the injected beams. The transition between a low- and a high-drift regime is given roughly by  $E_T \sim T_e$  ( $E_T = 1016$  eV with the parameters of Table 2, see equation (11) for details). If  $K_d < E_T$ , unstable waves are of the acoustic type and propagate parallel to the magnetic field. They can trap  $H^+$  and  $O^+$ , leading to phase-space vortices and ion solitary waves. On the other hand, if  $K_d > E_T$ , oblique cyclotron waves grow unstable which energize the  $O^+$  ions perpendicularly, leading to drifting conics in the  $O^+$  distribution. We have illustrated the point by detailing the results from two case runs: case A for the low-drift regime and case B for the high-drift regime. However, we performed other simulations in which the situation was not as clear-cut. For beam energies close to the transition energy,  $K_d \approx E_T$ , one simultaneously observes cyclotron waves and short packets of large amplitude acoustic waves. The latter dominate the first half of the simulation box as acoustic modes have a shorter spatial growth, while the former appear in the second half of the box consistently with their longer spatial growth. In time, the acoustic packets propagate into the “sea” of cyclotron waves where they appear to dissolve.

[37] For whichever case, energy is transferred from the protons to the oxygen ions via the instabilities. In the low-drift case, Table 4 shows that the drift energy  $K_d$  resulting from the instability is 2.2 times larger for the  $O^+$  ions than for  $H^+$  ions. For the high-drift case in Table 5,  $K_d$  for the  $O^+$  ions is 1.7 times larger than for the protons. Now satellite observations in the auroral acceleration zone have repeatedly indicated a larger energy for the  $O^+$  beam than for the  $H^+$  beam. For example, from 77 ion beams measured by FAST, *Moebius et al.* [1998] have compiled the peak energy of  $H^+$  and  $O^+$  and plotted the  $O^+$  to  $H^+$  energy ratio. The ratio is seen to be confined to a band between 1.5 and 4. Our simulations also show that the perpendicular temperature of the  $O^+$  beam is larger than that of the  $H^+$  beam. That is certainly true for the high-drift case illustrated in Figure 11 and Table 5, where  $K_{\perp} = 6.8$  for  $O^+$  and only 1.1 for  $H^+$ . Yet it is also true for the low-drift case in Table 4, which shows  $K_{\perp} = 1.9$  for  $O^+$  and only 1.1 for  $H^+$ . That is consistent with satellite observations that indicate a larger pitch angle for  $O^+$  than for  $H^+$  [*Collin et al.*, 1987; *Moebius et al.*, 1998].

[38] In the low-drift regime the continual injection of  $H^+$  and  $O^+$  beams drives acoustic waves to levels high enough to trap the ions, which results in phase-space vortices and ion solitary waves (ISWs). We have compared in section 3.1.2 the simulated ion holes to FAST measurements of ISWs [*McFadden et al.*, 2003]. Although the comparison suggests that ISWs are indeed ion holes due to the  $H^+$ - $O^+$  instability, there is some disagreement. The simulated ISWs have electric fields up to 280 mV/m, potentials of order 300 V, and propagate at speeds of order 200 km/s. The FAST estimates point to bigger structures with larger amplitude potentials (250 V to 900 V) and, most prominently, higher velocities (550 km/s to 1100 km/s). In fact, it was concluded that the propagation speed of ISWs is greater than the speed of the proton beam, a conclusion at variance with the one reached from Polar data. *Dombeck et al.* [2001] found velocities for ISWs which ranged from 100 km/s to 350 km/s and lay in the interval defined by the  $O^+$  and  $H^+$  beam speeds, similarly to our simulation results. There could be an instrumental error associated with the large-waveform distortion present in the FAST short antennae measurement. Another possibility in our view is that the discrepancy stems from the novel technique used in *McFadden et al.* [2003] which determines the amplitude of the potentials from the response of the electron spectrum. The method could have overestimated the potential amplitudes of the ISWs. This, in turn, led to overestimate their spatial extent and hence their propagation speeds.

[39] It is difficult to compare our results to those obtained by *Crumley et al.* [2001] because their simulation model is quite different from ours. Due to the choice of periodic boundaries along the magnetic field, the electrons, which move fast across the simulation box, are recycled many times during the course of a simulation run. From numerical values in their Table 1 one can estimate that, after  $10^4$  steps, an electron with initial thermal velocity  $v_e$  moving at constant speed would traverse 23 times the box. Now in order to maintain the instability, the authors have applied a large-scale steady electric field across the box corresponding to a potential drop of  $0.6 T_e/e$ , whereby the initially thermal electron can acquire an energy equal to at least  $14 T_e$ . The huge electron heating observed in the simulation, where  $T_e$

risks from 0.5 keV to 12 keV (see Figure 2), may stem from that assumed combination of dc field with periodic conditions. Possibly, the electrons are sufficiently accelerated for their drift to trigger a Buneman-type instability, as in a recent Vlasov study where the instability was driven by a drift between electrons and ions on the order of the electron thermal speed [Buechner and Elkina, 2006]. However, this is unlikely because of the polarity of the solitary waves reported. The Buneman instability leads to electron holes, thus positive potential humps, while Crumley *et al.* [2001] indicate only ion holes, or negative potentials. Whatever the source of the electron heating, the rise of  $T_e$  changes the regime in terms of “transition energy”. While the simulation run begins in the high-drift regime with the energy of the ion beams larger than  $E_T$  and the development of cyclotron waves, it eventually changes to the low-drift regime where the acoustic-acoustic coupling between the  $H^+$  and the  $O^+$  beams becomes possible. It is then, we presume, that they observe ion solitary waves. A telltale sign, the authors report that the dc electric field needs to be included in their simulations for the ion solitary waves to appear.

[40] The work of Main *et al.* [2006] has several similarities to ours, although the simulations are not PIC but are based on the Vlasov equation. The authors also use open boundaries and investigate the spatially inhomogeneous problem. There are two main differences yet. First, they include a strong double layer within the simulation box, so that their simulations start in the topside ionosphere. This shows that a BGK double layer is quasi-stable and leads to the continual acceleration of  $H^+$  and  $O^+$  ions into the cavity. We merely assume it herein. Secondly, their results are produced with a “reduced” 2D Vlasov code [Newman *et al.*, 2004], in which an algorithm is introduced to reduce the five-dimensional phase space that a true Vlasov description requires. In this algorithm the perpendicular direction is considered as a secondary physical dimension and the perpendicular velocity is described by means of a fixed perpendicular temperature. It is clear therefore that that type of simulation cannot consistently describe the wave-particle interaction in case of ion cyclotron waves, as we have in our case B herein where a perpendicular energization of the  $O^+$  ions takes place. Nevertheless, that limitation is not a major problem for the results presented in Main *et al.* [2006] since those were likely obtained in what we call the low-drift regime, similarly to our case A. The mention of cyclotron waves in the text notwithstanding, we believe that their simulations are dominated by acoustic waves and base our contention on the following evidences taken from their paper. (1) Their Figure 4 shows wavefronts oriented perpendicularly to the magnetic field in panel (a). Contrasting panels (a) and (b), one can equally see that  $E_{\parallel}$  is larger than  $E_{\perp}$ . Also, there is no herringbone display as exhibited in Figure 9 herein. (2) Their simulation box is likely too short to observe cyclotron growth. From Figure 9 herein one can see that a distance of 44 km (or  $600 \rho_H$ ) is required for the ion cyclotron waves to appear in the PIC simulations. Their box is just 40 km long, a distance which moreover includes the double layer and a section of ionosphere. In contrast with the long cyclotron growth length, the waves in their Figure 4 appear with a standoff of about 12 km from the double layer. That value turns out, in fact, to be the same

standoff which we observe in the PIC simulations for the acoustic instability. As illustrated in Figure 7 of this paper, the waves appear about  $160 \rho_H$  (or 12 km) from the left boundary.

[41] Finally, we should like to point out how complex is the plasma of the auroral acceleration cavity. Our model already includes four different particle populations: the hot electrons and the plasma sheet protons as well as the  $H^+$  and  $O^+$  beams. Yet although the latter are the two main components of auroral ion beams, there is also a helium contribution [e.g., Moebius *et al.*, 1998; McFadden *et al.*, 1999]. Clearly, in the study of ion streaming instabilities relevant to the cavity a next step could be to include a small  $He^+$  beam. Using the results herein as a baseline, one can add a helium beam of progressively increasing density. Because its drift velocity lays between the  $O^+$  and  $H^+$  beam speeds, a significant effect may be expected once the  $He^+$  beam reaches a sufficient density.

[42] **Acknowledgments.** The authors thank James McFadden for several discussions. The computations were performed on the SMP system of IBM at the Supercomputer Center in San Diego. The research work was supported by NASA under the grants NAG5-12989 and NNG05GL27G-06/08.

[43] Amitava Bhattacharjee thanks Bengt Eliasson and another reviewer for their assistance in evaluating this paper.

## References

- Bergmann, R., and W. Lotko (1986), Transition to unstable flow in parallel electric fields, *J. Geophys. Res.*, **91**, 7033.
- Bergmann, R., I. Roth, and M. K. Hudson (1988), Linear stability of the  $H^+-O^+$  two-stream interaction in a magnetized plasma, *J. Geophys. Res.*, **93**, 4005.
- Bostrom, R., G. Gustafsson, B. Holback, G. Holmgren, H. Koskinen, and P. Kintner (1988), Characteristics of solitary waves and weak double layers in the magnetospheric plasma, *Phys. Rev. Lett.*, **61**, 82.
- Bounds, S. R., R. Pfaff, S. F. Knowlton, F. S. Mozer, M. Temerin, and C. A. Kletzing (1999), Solitary potential structures associated with ion and electron beams near 1 RE altitude, *J. Geophys. Res.*, **104**, 28,709.
- Buechner, J., and N. Elkina (2006), Anomalous resistivity of current-driven isothermal plasmas due to phase space structuring, *Phys. Plasmas*, **13**, 082304.
- Cattell, C., et al. (1998), The association of electrostatic ion cyclotron waves, ion and electron beams and field-aligned currents: FAST observations of an auroral zone crossing near midnight, *Geophys. Res. Lett.*, **25**, 2053.
- Chaston, C. C., J. W. Bonnell, J. P. McFadden, R. E. Ergun, and C. W. Carlson (2002), Electromagnetic ion cyclotron waves at proton cyclotron harmonics, *J. Geophys. Res.*, **107**(A11), 1351, doi:10.1029/2001JA900141.
- Collin, H. L., W. K. Peterson, and E. G. Shelley (1987), Solar Cycle variation of some mass dependent characteristics of upflowing beams of terrestrial ions, *J. Geophys. Res.*, **92**, 4757.
- Crumley, J. P., C. Cattell, R. L. Lysak, and J. P. Dombeck (2001), Studies of ion solitary waves using simulations including hydrogen and oxygen beams, *J. Geophys. Res.*, **106**, 6007.
- Dombeck, J. P., C. Cattell, J. Crumley, W. K. Peterson, H. L. Collin, and C. Kletzing (2001), Observed trends in auroral zone ion mode solitary wave structure characteristics using data from Polar, *J. Geophys. Res.*, **106**, 19,013.
- Ergun, R. E., et al. (1998), FAST satellite observations of large-amplitude solitary structures, *Geophys. Res. Lett.*, **25**, 2041.
- Ergun, R. E., et al. (2002), Parallel electric fields in the upward current region of the aurora: Indirect and direct observations, *Phys. Plasmas*, **9**, 3685.
- Kintner, P. M., M. C. Kelley, and F. S. Mozer (1978), Electrostatic hydrogen cyclotron waves near one earth radius in the polar magnetosphere, *Geophys. Res. Lett.*, **5**, 139.
- Main, D. S., D. L. Newman, and R. E. Ergun (2006), Double layers and ion phase-space holes in the auroral upward-current region, *Phys. Rev. Lett.*, **97**, 185001, doi:10.1103/PhysRevLett.97.185001.
- McFadden, J. P., C. W. Carlson, R. E. Ergun, D. W. Klumppar, and E. Moebius (1999), Ion and electron characteristics in the auroral den-

- sity cavities associated with ion beams: No evidence for cold ionospheric plasma, *J. Geophys. Res.*, *104*, 14,671.
- McFadden, J. P., C. W. Carlson, R. E. Ergun, F. S. Mozer, L. Muschietti, I. Roth, and E. Moebius (2003), FAST observations of ion solitary waves, *J. Geophys. Res.*, *108*(A4), 8018, doi:10.1029/2002JA009485.
- Moebius, E., et al. (1998), Species dependent energies in upward directed ion beams over auroral arcs as observed with FAST TEAMS, *Geophys. Res. Lett.*, *25*, 2029.
- Newman, D. L., M. V. Goldman, R. E. Ergun, L. Andersson, and N. Sen (2004), Reduced Vlasov Simulations in Higher Dimensions, *Comput. Phys. Commun.*, *164*, 122.
- Roth, I., M. K. Hudson, and R. Bergmann (1989), Effects of ion two-stream instability on auroral ion heating, *J. Geophys. Res.*, *94*, 348.
- Temerin, M., K. Cerny, W. Lotko, and F. S. Mozer (1982), Observations of double layers and solitary waves in auroral plasma, *Phys. Rev. Lett.*, *48*, 1175.
- 
- L. Muschietti and I. Roth, Space Sciences Laboratory, University of California, 7 Gauss Way, Berkeley, CA 94720, USA. (laurent@ssl.berkeley.edu)